High dynamic range particle image velocimetry analysis of viscous inhalant flows

Cite as: Phys. Fluids **31**, 103605 (2019); https://doi.org/10.1063/1.5125813
Submitted: 27 August 2019 . Accepted: 10 October 2019 . Published Online: 24 October 2019

Aaron C. True, and John P. Crimaldi

Physics of Fluids ARTICLE scitation.org/journal/phf

High dynamic range particle image velocimetry analysis of viscous inhalant flows

Cite as: Phys. Fluids 31, 103605 (2019); doi: 10.1063/1.5125813
Submitted: 27 August 2019 • Accepted: 10 October 2019 •
Published Online: 24 October 2019

Aaron C. True[a] and John P. Crimaldi[b]

AFFILIATIONS

Civil, Environmental, and Architectural Engineering, University of Colorado Boulder, Boulder, Colorado 80309-0428, USA

[a]aaron.true@colorado.edu
[b]Author to whom correspondence should be addressed: crimaldi@colorado.edu

ABSTRACT

High dynamic velocity range (DVR) flows are challenging to measure with traditional double-pulse particle image velocimetry (PIV) since no single correlation time scale optimally resolves particle displacements over the entire DVR of interest. Inhalant flows are ubiquitous in engineering and biology and feature a high DVR as they draw viscous fluid through an orifice from a surrounding reservoir since large interior tube velocities rapidly attenuate with exterior distance from the inhalant orifice. We conducted a high-DVR PIV study of viscous inhalant flow hydrodynamics by developing and applying a multi-time-lag type processing scheme to construct DVR-enhanced flowfields. The algorithm adapts existing multi-time-lag type schemes into one that is well suited for slowly evolving flows with a persistent spatiotemporal structure. Correlation analyses between image pairs across two optimized time scales produce a pair of correlation maps well suited for resolution of targeted high and low measurement velocities. An evaluation map based on the best statistical relative strength of the local correlation peak amplitude and peak ratio is then used to spatially reconstruct a single DVR-enhanced velocity field with a DVR on the order of 1000:1. Numerical simulations show close agreement with measured flows everywhere following DVR enhancement, and the high-DVR PIV results reveal marked differences in the exterior flow kinematics and dynamics due to varying viscous and boundary interaction effects. The inlet velocity profiles at the tube orifice are highly sensitive to the Reynolds number within this range (1–100) and show notable departures from classically assumed uniform pipe entry profiles, impacting flow development lengths downstream.

I. INTRODUCTION

A. Inhalant flows

Inhalant flows are fundamental to engineered and biological systems.[1] They feature fluid drawn by suction from a surrounding reservoir through an inlet orifice and into an inhalant tube (Fig. 1). The exterior flow outside the inhalant tube is spatially distinct from the interior flow, the pipe flow inside the inhalant tube. The interior flow is comprised of the developing entrance flow just inside the inlet orifice, which transitions to the fully developed pipe flow further downstream.

The nondimensional flowfield induced by a round inhalant tube of inner diameter D is axisymmetric and $\mathbf{u}^* = [u^*, w^*]$, with radial ($r^*$) and axial ($z^*$) velocity components u^* and w^*. The flowfield is governed by the Navier-Stokes and continuity equations,

$$\frac{\partial \mathbf{u}^*}{\partial t^*} + \mathbf{u}^* \cdot \nabla^* \mathbf{u}^* = -\nabla^* p^* + \mathrm{Re}^{-1} \nabla^{*2} \mathbf{u}^* + \mathbf{g}^* \tag{1}$$

and

$$\nabla^* \cdot \mathbf{u}^* = 0. \tag{2}$$

Length, time, velocity, and pressure are nondimensionalized by D, D/w_o, w_o, and ρw_o^2, respectively, and $\mathbf{g}^* = D\mathbf{g}/w_o^2$. We denote vector quantities in bold face, scalar quantities in plain face, and nondimensional quantities with an asterisk. The flowfield is parameterized by the nondimensional wall thickness $d^* = d/D$ and extraction height $h^* = h/D$ and the tube Reynolds number $\mathrm{Re} = w_o D/\nu$ based on the average tube velocity $w_o = Q/A$, where Q is the volumetric flow rate and A is the tube cross-sectional area. Note that the advective time scale $T = D/w_o$ used to nondimensionalize time ($t^* = t/T$) can be rewritten as a transient time scale, $T = D/w_o = (D^2/\nu)/\mathrm{Re}$,

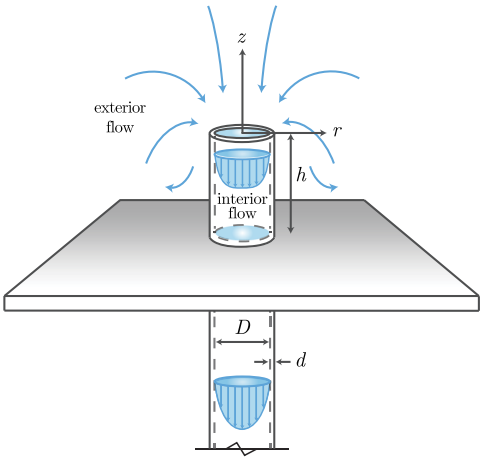

FIG. 1. Generic inhalant flow schematic. An inhalant tube protrudes some distance from a nearby boundary into an infinite reservoir. Viscous fluid is drawn through the inlet orifice under the action of suction. Laminar pipe flow follows downstream of the developing flow just inside the inlet orifice.

implying that the transient develops more quickly with increasing Re and reduced diffusive time scale D^2/ν.

Many aspects of the interior flow are well studied in a variety of contexts including pipe flow hydraulics[2,3] and biomedical flows.[4–6] Two canonical problems in the literature are the developing entrance flow just inside the inlet orifice (the hydrodynamic development length or pipe-entry problem[7]) and the fully developed laminar pipe flow that follows.[8] The Hagen-Poiseuille law describes steady laminar flow in an axisymmetric tube; the parabolic velocity profile $w(r)$ for the fully developed flow in a tube of inner radius R is given by

$$w(r) = -\frac{\Delta P}{4\mu}(R^2 - r^2), \tag{3}$$

where ΔP is the axial pressure gradient and μ is the dynamic viscosity. The volumetric flow rate Q is then $-\Delta P \pi r^4/8\mu$. Upstream of the fully developed pipe flow, the development length of the entry flow provides a measure of the distance required for the velocity profile in the tube to asymptote to the fully developed parabolic profile given by Eq. (3). Traditionally, the inlet profile is assumed to be uniform; in practice, this is unlikely and the actual profile will influence the development length.[9,10] Despite extensive numerical, experimental, and analytical studies of the development length problem, notable discrepancies remain between theory and experiment (see the review by Durst *et al.*[7]).

The exterior flow approaching an inlet orifice is of interest in a variety of contexts: pipettes,[11–13] aerosol and water samplers,[14,15] synthetic jets,[16] and organismal predation, feeding, and/or respiration processes.[17–25] While these studies explore many aspects of the exterior flow, most feature simplifications or complexities that complicate a mechanistic understanding of viscous inhalant flow hydrodynamics. Numerical modeling[1] recently quantified the effects of Re and extraction height h^* on the time-evolving exterior flow and showed marked differences in exterior flow kinematics and dynamics across the Re-h^* parameter space.

In the present study, we present measurements of the hydrodynamics of the coupled exterior and interior flows for laminar inhalant flows that develop following the impulsive start of constant volumetric inhalation Q. Measuring these flows presents experimental challenges, notably the high dynamic velocity range (DVR) associated with the difference between large interior tube velocities relative to the small exterior flow velocities, which rapidly attenuate with distance from the orifice.

B. Dynamic velocity range in PIV measurements

Particle image velocimetry (PIV) is a robust technique for measuring fluid velocity fields, most commonly via cross correlation analysis of two singly exposed images taken a short time apart.[26] The images capture the light scattered by seeding particles, passively entrained in the flow of interest. Image displacement fields are then computed by cross-correlating interrogation subwindows within the image pair. The cross correlation function is a random variable in space (Fig. 2), consisting of a maximum correlation peak corresponding to the image displacement (R_D) and background contributions from the convolution of the mean intensity (R_C) and random noise (R_F).[27]

The strength of R_D is proportional to a number of PIV system and flow-related parameters as

$$R_D \sim N_I F_I F_O \cdot F_{\Delta I} F_{\Delta O} \cdot F_C F_A, \tag{4}$$

where the effects of particle image ("seeding") density, in-plane and out-of plane loss-of-particle-pairs, in-plane and out-of-plane velocity gradients, flow curvature, and flow acceleration are characterized by N_I, F_I and F_O, $F_{\Delta I}$ and $F_{\Delta O}$, F_C, and F_A, respectively.[27,28] The ratio of the strongest correlation peak amplitude to the next strongest peak amplitude is called the peak ratio R_{ratio} and has been shown to strongly correlate with the measurement error[29] and thus the effective signal-to-noise ratio (SNR).

The strength of R_D strongly influences the dynamic velocity range (DVR) of a PIV measurement.[30] DVR is defined as

$$\mathrm{DVR} = \frac{U_{max}}{\sigma_u}, \tag{5}$$

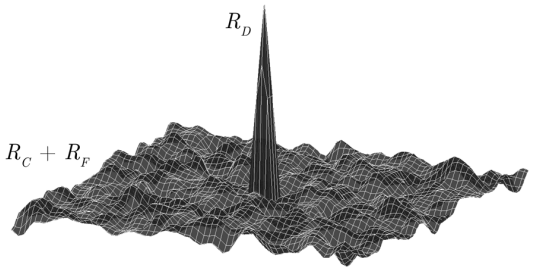

FIG. 2. Typical cross correlation function for two singly exposed images. The location of the correlation peak R_D with respect to the center of the interrogation subwindow gives the magnitude and direction of the in-plane image displacement. Adapted from Refs. 44 and 26.

where U_{max} is the maximum velocity and σ_u is the minimum resolvable velocity. Maximizing the PIV DVR can be achieved either by increasing the maximum velocity or by decreasing the minimum measurable velocity through the reduction of the measurement error. The total residual measurement error ϵ_{resid} is the sum of a bias error ϵ_{bias} (over or underestimation of velocity) and a random error ϵ_{rms} (measurement uncertainty).[31] The bias error can be largely mitigated through the optimization of the PIV system while the random error remains as the uncertainty of the PIV measurement.[32–34] The magnitude of the locally measured PIV velocity $|\mathbf{U}|$ is then

$$|\mathbf{U}| = \frac{|\mathbf{d}(\Delta t)|}{M_o \Delta t} + \frac{\epsilon_{resid}}{M_o \Delta t}, \tag{6}$$

where the particle image displacement $\mathbf{d}$ (px) is a function of the correlation time scale Δt (pulse or image separation) and M_o is the dimensionless optical magnification factor (L/L).

C. Maximizing PIV DVR

A range of interrogation methods and postprocessing schemes are utilized to enhance the DVR of PIV measurements. Advanced digital correlation and interrogation techniques such as multipass interrogation (first correlation pass is used to shift subwindows for subsequent interrogations) increase the DVR not only by enhancing correlation peak amplitude but also by reducing measurement uncertainty.[35] Grid refinement schemes (reduction of subwindow sizes during subsequent passes) and subwindow overlapping[36,37] offer further improvement through increased vector resolution, improving the dynamic spatial range (DSR = ratio of the largest to smallest observable lengthscales[30]), which is typically beneficial for resolving high-DVR flows. Finally, correlation peak amplitude degradation (broadening or even splitting) due to in-plane, subwindow scale velocity gradients can be mitigated using image (or window) deformation techniques in which subwindows are locally deformed for subsequent interrogations after a first correlation pass.[38–40]

In practice, PIV system optimization (Sec. II B 1) combined with modern correlation and interrogation schemes (Sec. II B 2) yields a maximum DVR of approximately 200:1 for a double-pulsed system.[41] This limitation is largely due to the coupling of the measurement DVR and DSR for a single global correlation time scale (the product of the two is constant for classical algorithms[30]). The DVR can be increased without sacrificing the DSR, however, by utilizing a multiframe (multi-time-lag, multiple-pulse-separation) technique.[42] The time-resolved, multiframe technique of Hain and Kähler locally selects a pair of images whose correlation time scale is optimized for particle displacements of 10 px. The time-resolved pyramid correlation scheme of Sciacchitano *et al.* creates an ensemble correlation map from a linear combination of correlations over a variety of image separation time scales. Lynch and Scarano utilized an advection-based, particle tracking-type approach to effectively increase the range of correlation time scales. A more recent generalized time-resolved approach by Persoons maximizes a vector quality metric based on the peak ratio and estimated uncertainty to select a locally optimized correlation time scale.

While these approaches increase the DVR by an order of magnitude or more, most were developed for time-resolved measurements of turbulent and complex flows and are typically computationally expensive. In the present study, we adapt existing multiframe approaches based on correlation peak amplitude and peak ratio criteria for local correlation optimization[28,43] to a multi-time-lag type DVR enhancement scheme applicable to slowly evolving flows with a persistent spatiotemporal structure. The approach detailed below is easy to implement and computationally inexpensive.

II. METHODOLOGY

A. Inhalant flow facility

PIV measurements were made in an index-matched inhalant flow facility (Fig. 3). The facility consisted of a cubic acrylic tank with a round inhalant tube protruding through the center of the bottom bed. A coupling system allowed for changing the extraction height (h^*, distance from bottom bed to orifice) and the inhalant tube diameter (D). The flow was drawn into the inlet orifice, through the inhalant tube, and discharged into an elevated receiving reservoir by a digital gear pump with adjustable volumetric flow rate Q. The pump was controlled with a transistor-transistor logic (TTL) signal from a National Instruments data acquisition board through the LabView interface to synchronize PIV data acquisition to transient flow development. The working fluid (mineral oil, Petro Canada, Paraflex HT9) and inhalant tube (borosilicate glass) had sufficiently similar indices of refraction ($n \approx 1.462$ and 1.470 at 20 °C, respectively) to mitigate laser refraction through the tube wall; this permitted PIV measurements of both the exterior and interior flowfields.

The inhalant flow facility was designed to minimize flow perturbations from a variety of sources. This was important due to the small target measurement velocities associated with rapid spatial attenuation of fluid velocity with distance from the inlet orifice. Buoyancy-driven, tank-scale circulation patterns were minimized by encapsulating the acrylic tank in fiberglass insulation. We used numerical simulations[1] to determine tank dimensions required to minimize boundary effects from the tank sidewalls and free surface; placing these boundaries at least $40D$ from the inlet orifice ensured negligible sidewall and free surface influences when compared to an open (infinite) domain. To ensure axisymmetric flow conditions throughout the entire experimental domain, the inhalant tube remained straight for a minimum of $150D$ downstream of the inlet orifice before transition to soft vinyl tubing and the discharge reservoir. Finally, *in situ* pump calibration yielded accurate volumetric flow rates Q for each experimental configuration.

B. PIV measurements

1. Correlation optimization: PIV system

Planar PIV measurements of time-evolving, axisymmetric inhalant flows were made in the r–z plane of the inhalant flow facility for different combinations of Re and extraction height h^* (Table I). The tank was seeded with particles (20 μm, 1.03 g/cc, and polyamide microspheres; Dantec Dynamics PSP-20) at 8–10 particles per interrogation subwindow (or 0.01 particles per pixel minimum). Adjustable light sheet optics (spherical focusing lens, cylindrical diverging lens doublet) spread a double-pulsed Nd:YAG laser (Quantel EverGreen 200; 532 nm, 200 mJ/pulse, and dual

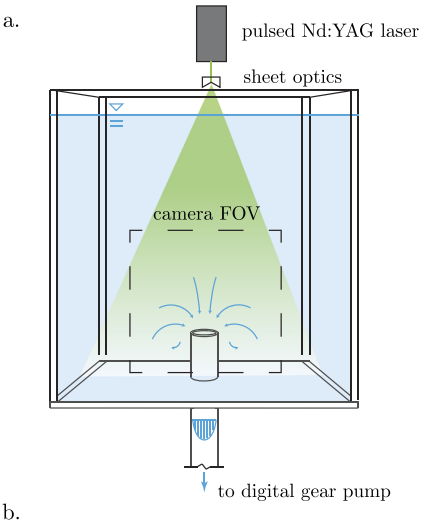

FIG. 3. Schematic (a) and photograph (b) of the inhalant flow facility.

cavity) beam into a thin sheet with an adjustable beam waist and Rayleigh range. An sCMOS camera (LaVision Imager sCMOS; 16 bit monochrome, 2160 × 2560, and 6.5 μm/px) imaged particles in the laser sheet at pulse separation times, which produced particle displacements of one-quarter (maximum one-half) the width of an interrogation subwindow (satisfying the "1/4" rule of Ref. 44). Relatively small seeding particles, low optical magnification factors M_o, and intermediate $f_\#$ (focal length/aperture diameter) produced typical diffraction-limited particle image diameters of 2.5–3.5 px.[45] A minimum particle signal level of 10 bits was maintained after all preprocessing, including background/time-series minimum subtraction (Ref. 26 and references therein).

2. Correlation optimization: PIV processing

PIV datasets were processed and analyzed using DaVis software (8.3, Lavision GmbH). Raw images were preprocessed (background subtraction of a time-series minimum intensity map and weak Gaussian smoothing) to improve particle fidelity and remove image artifacts associated with the presence of the inhalant tube (Fig. 4). A representative raw image is shown in Fig. 4(a) with a cartoon overlay of the tube for reference. The raw image itself with tube and background artifacts is shown in Fig. 4(b), and the resulting preprocessed image in Fig. 4(c) is then devoid of these artifacts. A typical interrogation subwindow [Fig. 4(d)] exhibits good particle signal levels and contrast with respect to the background, particle image (seeding) density, and particle image diameters.

Particle displacement fields were computed via fast-Fourier transform (FFT) based cross correlation. Best practices were utilized to maximize the measurement DVR including multipass (iterative) cross correlation schemes with overlapping (50%–75%) subwindows of decreasing sizes (64 px–32 px), adaptively shaped to local flow conditions. Despite velocimeter optimization and the use of modern correlation and interrogation schemes, PIV measurements optimized for particle displacements at a single correlation time scale were insufficient to capture the entire DVR of interest due to the large range of velocity scales present in the interior and exterior inhalant flow regions.

C. DVR enhancement: Multi-time-lag type postprocessing

1. DVR-enhancement algorithm

To enhance the DVR of our PIV measurements, we developed and applied a multi-time-lag type postprocessing scheme. For a single image dataset, two image acquisition time scales are constrained for optimal resolution of two target measurement velocities,

TABLE I. Summary of inhalant flow PIV datasets and related parameters.

Re	h^*	d^*	D (mm)	w_o (mm/s)	M (mm/px)	$1/f_I$ (s)	dt (ms)	Vectors (per D)
1	2	0.294	3.4	5.91	0.018	2.5	19.6[a]	23.14
10	0	0.294	3.4	59.11	0.018	0.25	2.5	23.14
10	2	0.294	3.4	59.11	0.018	0.25	2.5	23.14
10	40	0.294	3.4	59.11	0.018	0.25	2.5	23.14
100	2	0.077	15.6	128.85	0.078	0.5	4.9	24.70

[a]Max. dt allowable in software for double frame acquisition; ideal value is 25 ms.

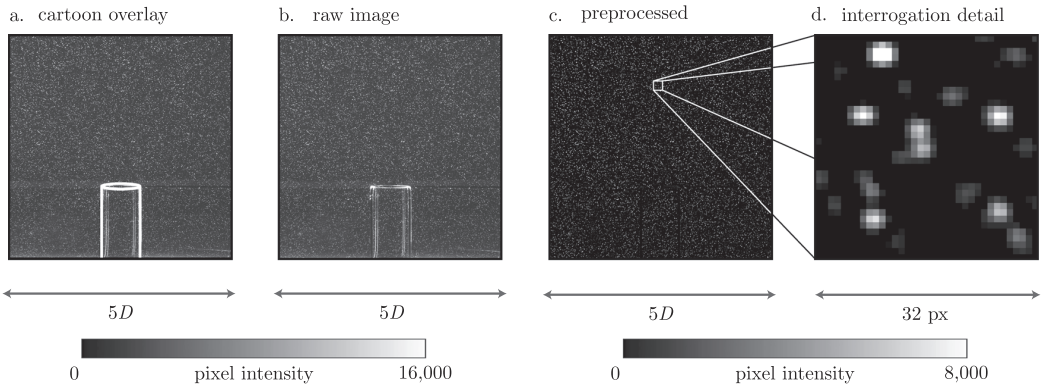

FIG. 4. Typical raw and preprocessed particle images showing a raw particle image with a cartoon overlay of the inhalant tube (a), the raw particle image (b), the preprocessed particle image (c), and a representative 32 px square interrogation subwindow (d).

one low and one high, such that each satisfies the "1/4" rule in a 32 px interrogation subwindow (Sec. II B 1) for particle displacements over a corresponding correlation time scale. In the present study, a series of double frame images with pulse separation time dt acquired at imaging frequency f_I (Fig. 5) provide the two correlation time scales (dt and $1/f_I$), which optimally resolve the target high (V_h) and low (V_l) measurement velocities and the cross-sectional average tube velocities w_o and 1% w_o, respectively (first row of Fig. 6). Correlation analyses between image pairs across each correlation time scale (dt and $1/f_I$) then produce two unique series of instantaneous correlation peak amplitude (R_D), correlation peak ratio (R_{ratio}), and particle displacement maps (second row of Fig. 6), which are well-suited for resolution of either the high (V_h) or low (V_l) target measurement velocity at discrete locations within the flow of interest. The correlation peak amplitude and peak ratio maps are then used to assess which correlation analysis is better suited for resolution of local flow conditions in terms of the local signal ($\sim R_D$) and SNR ($\sim R_{ratio}$). The quantitative assessment is based on an algorithmic evaluation map (double box in Fig. 6), which can be used to spatially interrogate the V_l- and V_h-optimized particle displacement fields in order to reconstruct a single DVR-enhanced displacement field.

Generation of the algorithmic evaluation map is illustrated for a representative dataset (Re = 100 and $h^* = 2$) in Fig. 7 and proceeds as follows:

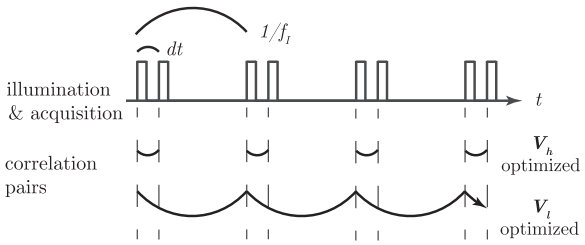

FIG. 5. PIV timing and correlation schematic for multi-time-lag type DVR-enhancement postprocessing.

1. Time-average of each series of instantaneous correlation peak amplitude (R_D) and peak ratio (R_{ratio}) maps from the V_l- and V_h-optimized correlation analyses.
2. To assess which correlation analysis is statistically better suited for the resolution of local flow conditions in terms of both the signal ($\sim R_D$) and SNR ($\sim R_{ratio}$), compute bidirectional ratios of the time-averaged peak amplitude [$R_{D,l}/R_{D,h}$ and $R_{D,h}/R_{D,l}$, Figs. 7(a) and 7(b)] and peak ratio [$R_{ratio,l}/R_{ratio,h}$ and $R_{ratio,h}/R_{ratio,l}$, Figs. 7(c) and 7(d)] maps.
3. For a given correlation analysis, select a threshold value for each ratio (e.g., $R_{D,l}/R_{D,h}$ and $R_{ratio,l}/R_{ratio,h}$ for the

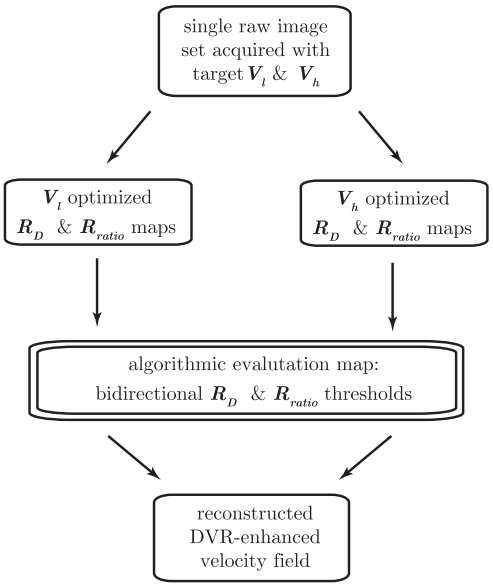

FIG. 6. Flow chart illustrating the multi-time-lag postprocessing scheme for PIV DVR enhancement.

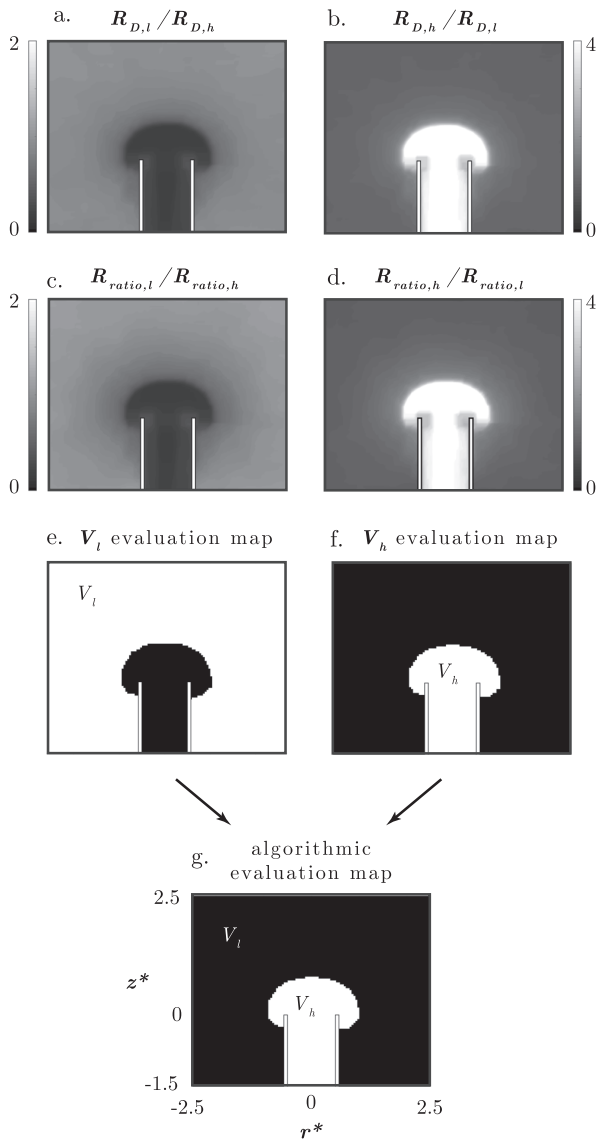

FIG. 7. Generation of the algorithmic evaluation map for high-DVR displacement field reconstruction. Ratios of the time-averaged correlation peak amplitude [(a) $R_{D,l}/R_{D,h}$ and (b) $R_{D,h}/R_{D,l}$)] and correlation peak ratio [(c) $R_{ratio,l}/R_{ratio,h}$ and (d) $R_{ratio,h}/R_{ratio,l}$)] yield the resulting V_l- and V_h-optimized evaluation maps [(e) and (f), respectively]. The combined algorithmic evaluation map (g) is used to spatially interrogate the V_l- and V_h-optimized displacement fields and reconstruct a single DVR-enhanced particle displacement field. See the step-by-step procedure in Sec. II C for detailed descriptions.

V_l-optimized correlation) and create a set of binary maps such that any ratio value above the threshold is set to one and all other values are set to zero. Threshold values selected should produce two binary maps that are mostly spatially coincident with each other and physically represent spatial locations where the given correlation analysis (e.g., V_l-optimized) better resolves local flow conditions in terms of the local measurement signal and SNR, consistent with the threshold values selected. Note that threshold values will always be near unity but are subjectively based on the spatiotemporal structure of the flow of interest and acceptable signal and noise tolerances for utilization of each velocity-optimization dataset.

4. Combine the two binary maps into a single binary evaluation map for a given correlation analysis [V_l- or V_h-optimized, Figs. 7(e) and 7(f), respectively]. In practice, add the two binary maps together, reassign all spatial indices with a value of two (physically representing locations where both the signal and SNR threshold criteria were satisfied) to one (white), and assign all other values to zero (black).
5. Finally, combine the separate V_l- and V_h-optimized evaluation maps into a single binary evaluation map [Fig. 7(g)]. In practice, reassign the unity values in the binary evaluation map from one correlation analysis (either the V_l- or V_h-optimized) to values of two and add the resulting V_l- and V_h-optimized evaluation maps. In the resulting map, values of zero, one, two, and three physically map to locations where (i) no correlation analysis satisfied all local signal and SNR criteria as constrained by the selected threshold values, (ii) one correlation analysis similarly satisfies local criteria (either the V_l- or V_h-optimized correlation), (iii) the other correlation analysis similarly satisfies local criteria, and (iv) both correlation analyses similarly satisfy all local signal and SNR criteria. Utilize a median filter to eliminate overlapping and/or null spaces within the combined evaluation map such that each spatial index maps to only one correlation analysis (either the V_l- or V_h-optimized). Rescale the resulting binary map to values of zero (black) and one (white) as shown in Fig. 7(g). This yields the final algorithmic evaluation map that physically maps spatial locations at which V_l- and V_h-optimized correlation analyses are best suited to resolve local flow conditions based on the imposed signal and SNR criteria.
6. Utilize the algorithmic evaluation map to spatially interrogate the V_l- and V_h-optimized displacement fields and reconstruct a single DVR-enhanced particle displacement field.

Note that if the V_l- and V_h-optimized correlations resolve different instants of time (Fig. 5), there is an implicit assumption that some time scale relevant to the flow development (e.g., the viscous diffusive time scale or the local advective time scale) is much greater than the temporal separation of the correlation analyses. Note that for our flow and PIV system parameters, a time series of double frame images provided the required optimal correlation time scales (as depicted in Fig. 5), but the same algorithm could be applied to a time-series of single frame images at different multiples of the imaging period $1/f_1$.

2. Applicability to flows of interest

When considering applicability of this DVR-enhancement scheme to a particular flow of interest, it is useful to determine what source of correlation degradation causes DVR limitation. Many factors that potentially degrade correlation peak amplitude R_D [Eq. (4)], which strongly influence the measurement DVR, can be largely

mitigated through velocimeter optimization and advanced interrogation and correlation techniques (see Ref. 28 for detailed discussion). For example, particle image density effects N_I are mitigated by optimal seeding densities of 0.01–0.02 particles per pixel. The effects of in-plane loss of particle pairs F_I and out-of-plane loss of particle pairs F_O can be mitigated through multipass window shifting techniques and by reducing out-of-plane displacements relative to the light sheet thickness, respectively. Similarly, the effect of in-plane gradients $F_{\Delta I}$ can be mitigated with window deformation techniques, while out-of-plane gradient effects $F_{\Delta O}$ cannot be mitigated through any advanced interrogation scheme. Finally, curvature effects F_C can be mitigated by window deformation techniques if the resulting gradients are constant over the interrogation window (similar to $F_{\Delta I}$ effects), while acceleration effects F_A specifically pertain to unsteady accelerations since convective acceleration effects are mitigated by combined multipass, window shifting, and window deformation techniques (similar to F_I and $F_{\Delta I}$ effects). The effects of F_A thus depend solely on the rate of change of acceleration with respect to time in addition to the measurement uncertainty.

Evaluating the flow of interest in light of the above considerations can inform what type of DVR-enhancement scheme is appropriate. For example, in the present study, the flows of interest are viscous inhalant flows that are axisymmetric with negligible unsteady accelerations (beyond the transient development period), and thus, the effects of F_O, $F_{\Delta I}$, $F_{\Delta O}$, and F_A do not directly degrade the correlation peak amplitude R_D. The effect of F_C due to flow curvature near the inlet orifice is largely mitigated by window deformation techniques since the associated gradients are large relative to the interrogation window size. Thus, the remaining factor that strongly influences the correlation peak amplitude and ultimately the measurement DVR is the effect of in-plane loss of particle pairs F_I. For this reason, multi-time-lag type DVR-enhancement schemes, such as the approach detailed above, are well suited for viscous inhalant flows. Furthermore, for these low-Re inhalant flows which evolve slowly in space and time following the initial transient startup, the instantaneous and time-averaged flowfields closely mirror each other such that the statistical (time-averaged) best correlation peak amplitude and peak ratio map obtained from the V_l- and V_h-optimized correlation analyses can be used to robustly reconstruct instantaneous, DVR-enhanced flowfields. Thus, high-DVR flows that (i) are well suited for multi-time-lag type DVR-enhancement schemes and (ii) have closely related instantaneous and time-averaged spatial structures will be well suited for the DVR-enhancement scheme detailed above. Other well-suited flows could include highly resolved laminar boundary layers, laminar round and slot jets, and Stokes flows. Note that there is a logical extension of the technique for high-DVR periodic flows satisfying similar conditions (linear waves, oscillating laminar pipe flows, vortex shedding behind obstacles, low Reynolds number synthetic jet-type type flows, etc.) in which phase-averaged correlation peak amplitude and peak ratio maps from low- and high-velocity optimized correlation analyses could be used to reconstruct high-DVR flowfields at individual phases of the flow.

D. Numerical modeling for validation

We utilized a numerical model to inform the design and construction of the inhalant flow facility and to validate our multi-time-lag postprocessing scheme for DVR enhancement. Numerical simulations were performed via finite element discretization of the incompressible Navier-Stokes and continuity equations [(1) and (2)]. Extensive details concerning mesh generation, finite element discretization, and solver implementation in the COMSOL MULTIPHYSICS software package[46] can be found by [1] The initial conditions were zero velocity and pressure everywhere. The flow was started impulsively by a boundary condition of laminar outflow from the downstream end of the inhalant tube with constant volumetric flow rate $Q = w_o A$ at time $t^* \geq 0$. The inhalant tube walls and the bottom bed were impermeable with no slip boundaries. The top and lateral boundary conditions were open boundaries through which fluid could enter and leave the domain without normal stress. In all comparisons of experimental and numerical results presented below, Re, h^*, d^*, initial and boundary conditions, and tank geometry were identically matched.

III. RESULTS

We use inhalant flow PIV measurements to demonstrate the efficacy of the multi-time-lag DVR enhancement scheme and to quantify the associated DVR gain. We then use this high-DVR PIV approach to explore the transient development of the exterior flow, effects of Re and h^* on exterior flow kinematics, and the effect of Re on the entry velocity profile at the inlet orifice and flow development length.

A. High-DVR PIV reconstruction

The DVR-enhancing reconstruction process is illustrated in Fig. 8 for a representative flow (Re = 100, $h^* = 2$, and $t^* = 10$). The top row shows normalized velocity magnitude fields that are correlation optimized for the resolution of the low (V_l = 1% w_o) and high ($V_h = w_o$) target measurement velocities. For the low-velocity optimization [Fig. 8(a)], small velocities of the exterior flow are well resolved, but larger velocities near and within the tube are noise dominated. Conversely, for the high-velocity optimization [Fig. 8(b)], large velocities of the interior flow are now well resolved, but the small velocities in the exterior flow quickly become noise dominated with distance from the orifice. In each case, the flow is well resolved in spatial regions where local velocities straddle the target measurement velocity. An algorithmic evaluation map is then used to select the best velocity optimization for a given spatial location based on local flow conditions. The resulting map for this flow case is shown in Fig. 8(c), where white and black regions denote the selected high and low-velocity optimization regions, respectively. By selectively combining results from each of the two correlation-optimized flowfields, the reconstructed velocity field [Fig. 8(d)] exhibits an enhanced DVR.

The DVR limitations of the low- and high-velocity optimized cases, and the enhanced DVR of the algorithmically reconstructed field, can be quantified in terms of the normalized strength of fluctuations in the PIV velocity measurements relative to the true signal. We define rms^* as the measurement rms normalized by the mean velocity; the metric is computed based on 1000 individual PIV realizations. Because the low-Re inhalant flows in this study exhibit negligible flow-related fluctuations, rms^* is a useful proxy for the ratio of measurement noise and true signal (i.e., an inverse SNR).

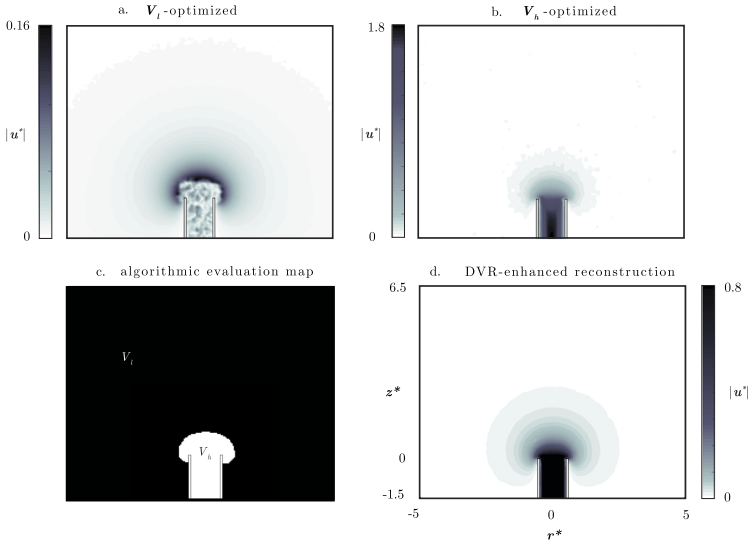

FIG. 8. Representative DVR-enhanced velocity field reconstruction showing separate fields optimized for resolution of target low (a) and high (b) velocities, the associated algorithmic evaluation map (c), and the reconstructed high-DVR velocity field (d).

This is further validated as the average rms fluctuations of the V_l- and V_h-optimized displacement fields (0.08 px and 0.03 px, respectively) are shown to be on the order of satisfactory PIV measurement uncertainties utilizing best practices (≤0.1 px, e.g., Ref. 26).

Figure 9 compares centerline axial profiles of the normalized velocity magnitude from the PIV measurements (symbols) and numerical simulations (lines). The data in the first two rows are for the low- and high-velocity optimizations, respectively. For these two cases, associated rms^* profiles are shown in the right column. The final row shows the reconstructed high-DVR velocity field. The measured V_l-optimized velocities [Fig. 9(a)] match the numerical results closely in the far-field before diverging rapidly as velocities increase near the inhalant tube orifice ($z^* = 0$). The close match corresponds to the spatial region covered by the DVR which contains the target measurement velocity (1% w_o). However, the profiles diverge as in-plane loss-of-particle-pairs due to high particle displacements near the inlet orifice degrade the correlation peak amplitude [Eq. (4)], increasing the measurement uncertainty and reducing the measurement accuracy. This is reflected in the corresponding rms^* profile [Fig. 9(b)], which is minimized in the far-field where the correlation is optimized and increases by an order of magnitude near the inlet orifice as the correlation degrades. Similarly, the measured V_h-optimized velocities [Fig. 9(c)] match the numerical profile closely in the near-field (inside the inhalant tube and just outside the inlet orifice) before diverging rapidly as velocities decrease in the far-field. Here, the profiles diverge due to vanishingly small particle displacements in the far-field, which causes the residual error term in the PIV measurement [Eq. (6)] to dominate the true velocity. This is again reflected in the corresponding rms^* profile [Fig. 9(d)], which is minimized in the near-field where the correlation is optimized and increases with increasing z^* as a result of the increased measurement error. In contrast, the high-DVR reconstruction closely matches the numerical solution along the entire length of the profile, including at the axial centerline [Fig. 9(e)] and throughout the flowfield of interest [Fig. 9(f)].

To estimate the DVR of the V_l- and V_h-optimized velocity fields and the high-DVR reconstructed field, a conservative criterion of $rms^* \leq 0.1$ (i.e., ~SNR ≥ 10) was used to delineate the minimum resolvable velocity [σ_u, Eq. (5)] for the V_h-optimized field and the maximum resolvable velocity [U_{max}, Eq. (5)] for the V_l-optimized field. Note that this closely coincides spatially with both the point at which each rms^* profile begins increasing or peaking [Figs. 9(a) and 9(b)] and the algorithmic evaluation map computed and utilized for reconstruction (Fig. 7). The estimated DVR for the V_l-optimized field is 50:1, based on the maximum and minimum velocities of 10% w_o and 0.2% w_o, respectively. Similarly, the estimated DVR for the V_h-optimized displacement field is 20:1, based on the maximum and minimum velocities of $2w_o$ and 10% w_o, respectively. In each of these cases, the estimated DVR is an order of magnitude lower than 200:1, an attainable value when using double-pulse PIV with modern correlation and interrogation schemes.[41] Note that these DVR estimates are conservatively based on a criterion of $rms^* = 0.1$ and also contain some velocity resolution overlap between V_l- and V_h-optimized cases. Note also that both cases are DVR constrained by the flow of interest in addition to issues related to correlation peak degradation and measurement uncertainty discussed above. For example, in the V_l case, σ_u was constrained to the minimum velocity observed in the field-of-view (approximately 0.2% w_o), and similarly in the V_h case, U_{max} was constrained near $2w_o$, the maximum interior tube velocity. Nonetheless, utilizing these conservative DVR estimates, the DVR of the reconstructed velocity field was 1000:1 ($U_{max}/\sigma_u = 2w_o/0.2\%\ w_o$).

B. HDR PIV results: Viscous inhalant flow hydrodynamics

Here, we present high-DVR PIV results for different Reynolds numbers (Re = 1, 10, and 100) and extraction heights (bed-flush

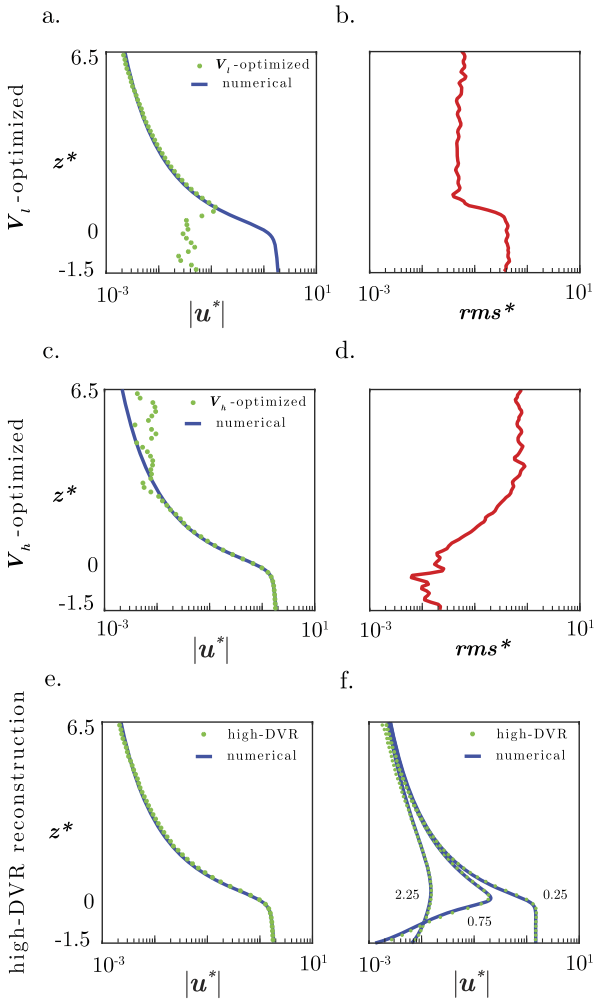

FIG. 9. Comparison of centerline axial profiles of normalized velocity magnitude from the PIV measurements (symbols) and numerical simulations (lines) for the V_l optimization (a), V_h optimization (c), and reconstruction (e). Corresponding profiles of rms^* are shown for each of the two optimizations (b) and (d). Noncenterline axial profile comparisons of normalized velocity magnitude taken along $r^* = 0.25$, 0.75, and 2.25 are also shown in (f).

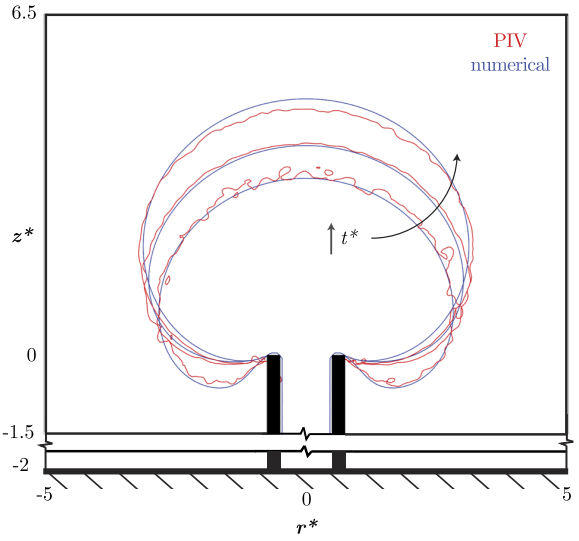

FIG. 10. Transient development of the flowfield as represented by evolution of the 1% w_o contours for Re = 10 and $h^* = 2$. The bottom bed is denoted in cross-hatch, and the inhalant tube sidewalls are shown in black at $r^* = \pm 0.5$. The blue and red curves represent numerical and high-DVR PIV results, respectively. The three sets of curves are for $t^* = 1$, 10, and 100. Note the comparatively noisy curves at $t^* = 1$ due to the large unsteady accelerations during the transient start-up period.

case $h^* = 0$, near-bed case $h^* = 2$, and unbounded case $h^* = 40$) (Table I). For the exterior flow, we quantify "regions of influence" (RoI), defined here as the volume of fluid bounded by a given velocity magnitude contour at a given time. The RoIs are used to quantify the spatial distribution and temporal development of the exterior flowfield induced by the inhalant tube flow.

1. Exterior flow: Transient development

To visualize the transient response of the exterior flow after the impulsive start of inhalation ($t^* = 0$), we present the time evolution of the 1% RoI contours for a single intermediate case (Re = 10 and $h^* = 2$) in Fig. 10. The 1% numerical and experimental RoIs are plotted at the end of the rapid transient development ($t^* = 1$), at an intermediate time following the establishment of the viscous structure of the flowfield ($t^* = 10$), and into the long-time behavior of the flowfield ($t^* = 100$). Conceptually, the transient response is composed of two parts. First, an inviscid, elliptic component sets up instantaneously and is related to a steady sink flow with the exception that it must satisfy the no-slip boundary condition along solid surfaces and must match the distributed and directional flow at the orifice. Second, a viscous component diffuses radially outward over time.

For this intermediate flow case (Re = 10), at $t^* = 1$, the flow consists primarily of the inviscid elliptic response with radial, sink-like inflow. As time progresses, the viscous structure becomes apparent by $t^* = 10$ after the unsteady, viscous, diffusive component has set up, causing the RoIs to enlarge and propagate axially upwards. The effects continue to the long-time state of the flow ($t^* = 100$). The structural changes in the flow throughout the transient development emphasize a fundamental feature of low-Re inhalant flows: the competition between advection of momentum toward the orifice and viscous diffusion away from the orifice. As detailed below, the relative strength and interplay of these two components depend on nondimensional time, Re, d^*, and h^*.

2. Exterior flow: Effects of Re and bed location

We present the effect of Re (Fig. 11) and h^* (Fig. 12) on the spatial structure of the exterior flow at $t^* = 10$, a time large compared to the time scale of rapid transient development ($t^* \leq 1$). Although

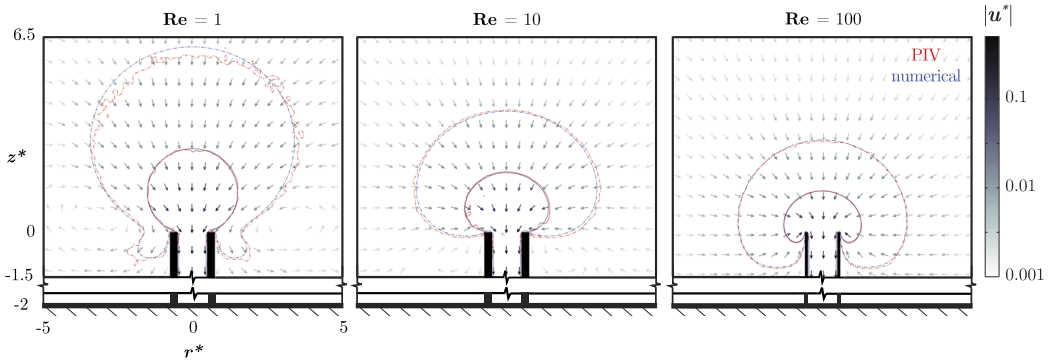

FIG. 11. Effect of Re for a fixed bed location (near-bed, h^* = 2) at t^* = 10. Inhalant tube, bottom bed, and RoI contours represented as in Fig. 10. Velocity direction and magnitude from high-DVR reconstructed velocity fields are indicated by arrow orientation and coloration, respectively.

exterior flows continue to slowly develop after t^* = 10, particularly for the Re = 1 case, the basic structural features of the viscous flow field are well established. In Fig. 11, Re varies from 1 (left panel) to 10 (middle panel) to 100 (right panel) for a fixed extraction height (h^* = 2), and in Fig. 12, h^* varies from 0 (bed-flush, left panel) to 2 (near-bed, middle panel) to 40 (unbounded, right panel) for a fixed Re = 10. To best visualize the large DVR, normalized velocity magnitudes ($\mathbf{u}^*$) are displayed on a logarithmic scale. In each figure, we present numerical and experimental RoIs for $|\mathbf{u}^*|$ = 0.05 and $|\mathbf{u}^*|$ = 0.01, indicating where velocities have decayed to 5% and 1% of w_o.

For a fixed extraction height of h^* = 2 and nondimensional time t^* = 10 (near-bed case, Fig. 11), varying Re results in structural changes in the flow field. The enhanced effects of viscous diffusion at low Re (Fig. 11, left panel) become evident in the increased spatial extent of the 1% RoI due to viscous entrainment, producing preferential downward, axial (z-axis) flow of an ever increasing volume of fluid. Conversely, reduced viscous effects in the highest Re case (Fig. 11, right panel) cause inward advection of momentum to dominate outward viscous diffusion, retarding the entrainment processes seen in the low Re case, and trapping the flow in a state suggestive of an inviscid sink flow with radial inflow and nearly spherical RoIs. The spatial structure of the intermediate Re case (Fig. 11, middle panel) is clearly a product of both viscous and inertial influences on the flow. Note that the lobes near the inlet orifice in the 1% RoI of the low Re case (Fig. 11, left panel) are a result of viscously entrained fluid that ultimately bypasses the inlet orifice and is deflected radially by the bottom bed. There is a stagnation streamline which terminates on the wall of the inhalant tube at the inlet orifice, separating inhaled from bypassed fluid.[1] Examination of the velocity vectors for the intermediate Re case (Fig. 11, middle panel) reveals similar flow structures, even though it is not readily evident in the RoIs. These effects are greatly diminished and nearly imperceptible in the high Re case (Fig. 11, right panel). Note that while for all cases, the agreement between the numerical and experimental data is remarkably close, the agreement suffers somewhat in the far-field for the Re = 1 case (Fig. 11, right panel). There are two primary reasons for this. First, the dimensional target measurement velocity is 59.1 μm/s (1% w_o, Table I), making it highly susceptible to perturbations from background flows, and second, vanishingly small

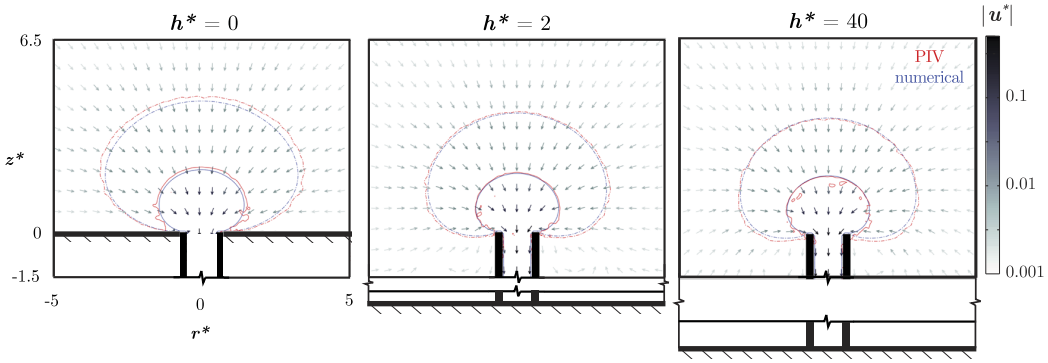

FIG. 12. Effects of the bed-location for fixed Re = 10 at t^* = 10. Inhalant tube, bottom bed, RoI contours, and velocity direction and magnitude represented as in Fig. 11.

particle displacements in the far-field cause the residual error term to dominate the true velocity term here [Eq. (6)], resulting in a noisier contour.

For a fixed intermediate Re = 10 and nondimensional time t^* = 10, varying the extraction height (Fig. 12) again results in structural changes in the flowfield due to varying levels of interaction with the bottom bed. In the bed-flush case (h^* = 0, Fig. 12, left panel), there is radial inflow toward the inlet orifice, which attenuates rapidly with distance from the orifice. The no-slip condition along the bottom bed gives rise to a boundary layer that somewhat retards inflow along the bed, causing preferentially axial inflow along the z-axis. In contrast, in the unbounded case (h^* = 40, Fig. 12, right panel), the influence of the bottom bed is effectively eliminated and the inflow is primarily radial with small recirculation zones confined near the inhalant tube wall. While the RoIs for the near-bed case (h^* = 2, Fig. 12, middle panel) look qualitatively similar to those of the unbounded case (Fig. 12, right panel), the velocity vectors show that the recirculation zones present in the unbounded case have enlarged laterally away from the inhalant tube walls, evidence of increased interaction between viscously entrained, bypassing fluid and the bottom bed. Note that for this intermediate Re = 10, the spatial structure and extent of the 1% RoI are sensitive to nondimensional wall thickness d^* across all t^* and for nonzero h^* (e.g., middle and right panels of Fig. 12 vs t^* = 10 curves in middle panels of Figs. 8 and 9 of Ref. 1).

3. Interior flow: Entry profile and development length

The effect of Re on the velocity profile at the inlet orifice (entry profile) is shown in Fig. 13(a). Modeled (numerical, lines) and measured (high-DVR PIV, symbols) normalized entry velocity profiles are shown at z^* = 0 for Re = 1 (blue) and Re = 100 (red). The fully developed analytical laminar profile (thin black line) is also shown for reference. In both the Re = 1 and Re = 100 cases, fluid nearing the inlet orifice experiences convective acceleration axially and radially. In the lower-Re case, however, axial diffusion of momentum upstream of the orifice, combined with enhanced viscous boundary layers along the inhalant tube walls, allows the entry profile to already assume the parabolic functional shape of fully developed laminar pipe flow, with the exception of reduced centerline velocities and a necessarily wider profile to conserve mass flux through the orifice. In contrast, in the more inviscid case, downstream advection retards the effects of upstream diffusion and the interaction of the wall boundary layer with the combined effects of convective acceleration near the orifice causes the centerline velocity peak to be greatly reduced and to bifurcate into two off-center peaks, symmetric about the centerline. This "profile inversion" is consistent with recent studies, providing the first experimental observations of this phenomenon for laminar pipe entry flows at intermediate Re.[47,48] Note that both profiles are categorically nonuniform in contrast to a vast majority of historical studies (e.g., Ref. 7) and affect the flow development length accordingly.[23]

Flow development length as a function of Re is also explored in Fig. 13. In Fig. 13(a), the normalized velocity magnitude profiles plotted at z^* = −1.5 [lower extent of the camera field of view (FOV)] show that the Re = 1 flow is already full developed (perfectly overlays the Poiseuille profile here), while the Re = 100 flow has developed into a parabolic profile but has yet to assume the fully developed laminar profile. The centerline velocity in the Re = 1 case reaches

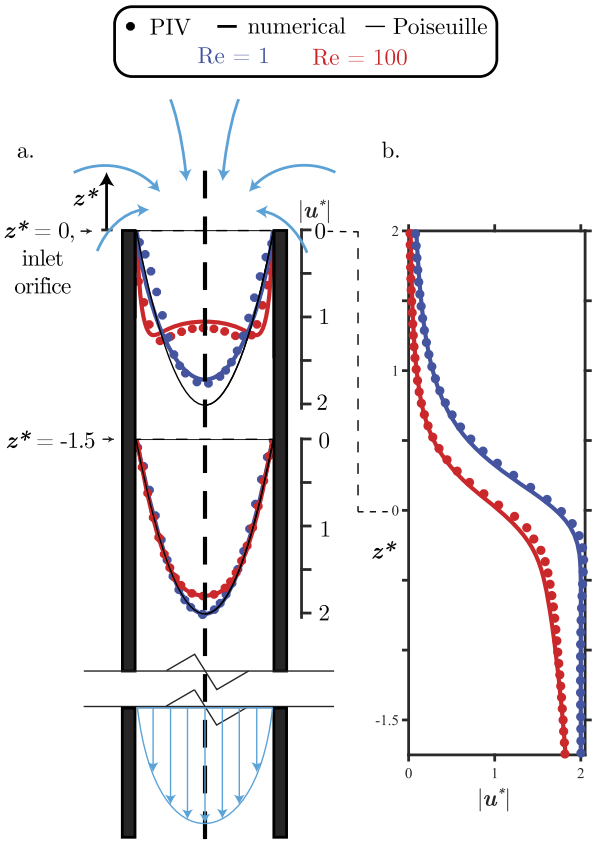

FIG. 13. Spatial development of the exterior approach and interior pipe flows well beyond the start of impulsive inhalation (t^* = 100) for the near-bed case (h^* = 2). Inhalant tube sidewalls denoted as black rectangles. (a) Normalized cross-sectional velocity magnitude profiles at z^* = 0 (inlet orifice) and at z^* = −1.5. (b) Centerline normalized velocity magnitude profiles from the approach ($z^* \geq 0$) through the entry and development ($z^* \leq 0$) flow regions.

99% of the fully developed value ($2w_o$) $0.559D$ downstream of the orifice, while the Re = 100 case continues asymptoting toward the fully developed state [Fig. 13(b)]. Note that the measured development length for Re = 1 is 12% lower than that predicted by the analytical correlation of Durst *et al.*, which was fit to the results of numerical simulations based on an imposed uniform entry profile. As the authors noted, the poor performance of the analytical development length expression for $1 \leq \text{Re} \leq 100$ stems not only from the unrealistic entry profile but also due to the fact that the low-Re asymptote only accounts for diffusive effects, while the high-Re asymptote considers only the effects of axial advection and radial diffusion. For these low-Re inhalant flows, advection and diffusion of fluid momentum both axially and radially clearly affect flow dynamics and kinematics in the approach region upstream of the inlet orifice, influencing subsequent flow development downstream. Note that the effects of Re on both the entry profile and development length discussed above should be considered in light of the

nearby bottom bed, which also influences exterior flow kinematics and dynamics (Sec. III B 2, Fig. 12).

IV. CONCLUSIONS

We developed and applied a multi-time-lag type postprocessing scheme that offers DVR enhancement, conservatively up to 1000:1 for high-DVR, reconstructed flowfields. Our scheme utilizes a combined correlation peak amplitude and peak ratio metric and is well suited for studying high-DVR flows with a persistent spatiotemporal structure. The algorithm is easy to implement, computationally inexpensive, and useful for studying slowly evolving, high-DVR flows relevant in ecology, biology, and engineering.

Utilizing this DVR-enhancement scheme, we conducted a high-DVR PIV study of the time-evolving hydrodynamics of low-Re inhalant flows, showing marked differences in exterior flow kinematics and dynamics as a result of varying viscous and boundary interaction effects. The inlet velocity profile at the inhalant tube orifice was also shown to be highly sensitive to Re in this range (1–100) with associated impacts on the flow development length in the downstream pipe. These results suggest that inhalant tube Re and geometry can be tuned to produce desired flow dynamics and kinematics for engineers and organisms alike.

ACKNOWLEDGMENTS

We thank Pete Jumars for motivation to investigate these flows and for many fruitful discussions. We wish him a happy retirement.

This work was supported by the NSF (USA), Grant No. OCE 1260199, to J.P.C.

REFERENCES

[1]A. C. True and J. P. Crimaldi, "Hydrodynamics of viscous inhalant flows," Phys. Rev. E **95**, 053107 (2017).
[2]C. Colebrook and C. White, "Experiments with fluid friction in roughened pipes," Proc. R. Soc. London, Ser. A **161**, 367–381 (1937).
[3]Z. Xu, S. Song, F. Xin, and T. J. Lu, "Mathematical modeling of stokes flow in petal shaped pipes," Phys. Fluids **31**, 013602 (2019).
[4]C. A. Taylor and M. T. Draney, "Experimental and computational methods in cardiovascular fluid mechanics," Annu. Rev. Fluid Mech. **36**, 197–231 (2004).
[5]M. C. Brindise and P. P. Vlachos, "Pulsatile pipe flow transition: Flow waveform effects," Phys. Fluids **30**, 015111 (2018).
[6]K. Pradhan and A. Guha, "Fluid dynamics of oscillatory flow in three-dimensional branching networks," Phys. Fluids **31**, 063601 (2019).
[7]F. Durst, S. Ray, B. Ünsal, and O. Bayoumi, "The development lengths of laminar pipe and channel flows," J. Fluids Eng. **127**, 1154–1160 (2005).
[8]S. P. Sutera and R. Skalak, "The history of Poiseuille's law," Annu. Rev. Fluid Mech. **25**, 1–20 (1993).
[9]B. Atkinson, M. Brocklebank, C. Card, and J. Smith, "Low Reynolds number developing flows," AIChE J. **15**, 548–553 (1969).
[10]R.-Y. Chen, "Flow in the entrance region at low Reynolds numbers," J. Fluids Eng. **95**, 153–158 (1973).
[11]J. L. Gay-Lussac, *Instruction sur l'essai du Chlorure de Chaux* (Ve Thuau, 1830).
[12]A. T. Shohl, "A pipet for micro-analyses," J. Am. Chem. Soc. **50**, 417 (1928).
[13]M. Köhn, "Beiträge zur theorie und praxis der mechanischen bodenanalyse," Ph.D. thesis, Forstliche Hochschule, Eberswalde, 1928.
[14]S. K. Zaripov, L. Zigangareeva, and O. Kiselev, "Aerosol aspiration into a tube from a calm medium," Fluid Dyn. **35**, 242–246 (2000).
[15]S. Dunnett and X. Wen, "A numerical study of the sampling efficiency of a tube sampler operating in calm air facing both vertically upwards and downwards," J. Aerosol Sci. **33**, 1653–1665 (2002).
[16]B. Smith and G. Swift, "A comparison between synthetic jets and continuous jets," Exp. Fluids **34**, 467–472 (2003).
[17]H. Lewis, A. Foster, B. Mullan, R. Cox, and R. Clark, "Aerodynamics of the human microenvironment," Lancet **293**, 1273–1277 (1969).
[18]C. Jorgensen, "The bivalve pump," Mar. Ecol.: Prog. Ser. **34**, 69–77 (1986).
[19]S. G. Monismith, J. R. Koseff, J. K. Thompson, C. A. O'Riordan, and H. M. Nepf, "A study of model bivalve siphonal currents," Limnol. Oceanogr. **35**, 680–696 (1990).
[20]H. U. Riisgard and P. S. Larsen, "Filter-feeding in marine macro-invertebrates: Pump characteristics, modelling and energy cost," Biol. Rev. **70**, 67–106 (1995).
[21]G. S. Settles, "Sniffers: Fluid-dynamic sampling for olfactory trace detection in nature and homeland security—The 2004 freeman scholar lecture," J. Fluids Eng. **127**, 189–218 (2005).
[22]S. Van Wassenbergh and P. Aerts, "Aquatic suction feeding dynamics: Insights from computational modelling," J. R. Soc., Interface **6**, 149–158 (2009).
[23]P. A. Jumars, "Boundary-trapped, inhalant siphon and drain flows: Pipe entry revisited numerically," Limnol. Oceanogr.: Fluids Environ. **3**, 21–39 (2013).
[24]S. Yaniv, D. Elad, and R. Holzman, "Suction feeding across fish life stages: Flow dynamics from larvae to adults and implications for prey capture," J. Exp. Biol. **217**, 3748–3757 (2014).
[25]K. T. Du Clos, I. T. Jones, T. J. Carrier, D. C. Brady, and P. A. Jumars, "Model-assisted measurements of suspension-feeding flow velocities," J. Exp. Biol. **220**, 2096–2107 (2017).
[26]M. Raffel, C. E. Willert, S. Wereley, and J. Kompenhans, *Particle Image Velocimetry: A Practical Guide* (Springer, 2013).
[27]R. D. Keane and R. J. Adrian, "Theory of cross-correlation analysis of PIV images," Appl. Sci. Res. **49**, 191–215 (1992).
[28]R. Hain and C. Kähler, "Fundamentals of multiframe particle image velocimetry (PIV)," Exp. Fluids **42**, 575–587 (2007).
[29]J. J. Charonko and P. P. Vlachos, "Estimation of uncertainty bounds for individual particle image velocimetry measurements from cross-correlation peak ratio," Meas. Sci. Technol. **24**, 065301 (2013).
[30]R. Adrian, "Dynamic ranges of velocity and spatial resolution of particle image velocimetry," Meas. Sci. Technol. **8**, 1393 (1997).
[31]H. Huang, D. Dabiri, and M. Gharib, "On errors of digital particle image velocimetry," Meas. Sci. Technol. **8**, 1427 (1997).
[32]B. Wieneke, "PIV uncertainty quantification from correlation statistics," Meas. Sci. Technol. **26**, 074002 (2015).
[33]D. R. Neal, A. Sciacchitano, B. L. Smith, and F. Scarano, "Collaborative framework for PIV uncertainty quantification: The experimental database," Meas. Sci. Technol. **26**, 074003 (2015).
[34]A. Boomsma, S. Bhattacharya, D. Troolin, S. Pothos, and P. Vlachos, "A comparative experimental evaluation of uncertainty estimation methods for two-component PIV," Meas. Sci. Technol. **27**, 094006 (2016).
[35]J. Westerweel, D. Dabiri, and M. Gharib, "The effect of a discrete window offset on the accuracy of cross-correlation analysis of digital PIV recordings," Exp. Fluids **23**, 20–28 (1997).
[36]C. Willert, "Stereoscopic digital particle image velocimetry for application in wind tunnel flows," Meas. Sci. Technol. **8**, 1465 (1997).
[37]D. P. Hart, "Super-resolution PIV by recursive local-correlation," J. Visualization **3**, 187 (2000).
[38]H. Huang, H. Fiedler, and J. Wang, "Limitation and improvement of PIV. Part II: Particle image distortion, a novel technique," Exp. Fluids **15**, 263–273 (1993).
[39]F. Scarano, "Iterative image deformation methods in PIV," Meas. Sci. Technol. **13**, R1 (2001).
[40]J. Westerweel, "On velocity gradients in PIV interrogation," Exp. Fluids **44**, 831–842 (2008).
[41]J. Westerweel, G. E. Elsinga, and R. J. Adrian, "Particle image velocimetry for complex and turbulent flows," Annu. Rev. Fluid Mech. **45**, 409–436 (2013).

[42]T. Persoons, "Time-resolved high-dynamic-range particle image velocimetry using local uncertainty estimation," AIAA J. **53**, 2164 (2014).
[43]C. J. Kähler and J. Kompenhans, "Fundamentals of multiple plane stereo particle image velocimetry," Exp. Fluids **29**, S070–S077 (2000).
[44]R. D. Keane and R. J. Adrian, "Optimization of particle image velocimeters. I. Double pulsed systems," Meas. Sci. Technol. **1**, 1202 (1990).
[45]C. J. Kähler, S. Scharnowski, and C. Cierpka, "On the resolution limit of digital particle image velocimetry," Exp. Fluids **52**, 1629–1639 (2012).
[46]D. W. Pepper and X. Wang, "Benchmarking COMSOL multiphysics 3.5a—CFD problems," paper presented at the 2009 COMSOL Conference, 2009.
[47]A. Reci, A. J. Sederman, and L. F. Gladden, "Experimental evidence of velocity profile inversion in developing laminar flow using magnetic resonance velocimetry," J. Fluid Mech. **851**, 545–557 (2018).
[48]H. D. Haustein and B. Kashi, "Distortion of pipe-flow development by boundary layer growth and unconstrained inlet conditions," Phys. Fluids **31**, 063602 (2019).